

Contents

<b>S1 Seismic power methodology</b>	<b>S1</b>
S1.1 Temporal reconstruction . . . . .	S1
S1.2 Evaluating instrumental bias in $\delta t$ interpretation . . . . .	S1
S1.3 Evaluating the potential bias from impulsive events contribution to seismic power . . . . .	S2
S1.4 Evaluating the anthropogenic signature influence on sub-diurnal timescales . . . . .	S2
S1.5 Evaluating the spatial sensitivity of the seismic record . . . . .	S2
<b>S2 Theoretical channel properties</b>	<b>S4</b>
S2.1 Evaluating theoretical channels dynamics with R�othlisberger (1972)' equations . . . . .	S4
S2.2 Evaluating theoretical melt and creep rates with Hooke (1984)' equations . . . . .	S4
<b>S3 Codes for seismic processing</b>	<b>S6</b>
S3.1 Remove instrumental response with SAC . . . . .	S6
S3.2 Compute PSD with Python . . . . .	S6

**S1 Seismic power methodology**

**S1.1 Temporal reconstruction**

We show in Fig. S1 the seismic stations used to reconstruct the 'virtual station' seismic power . The overlapping period of mid-October 2017 is used to adjust, over a 10 days time window, the GDA seismic power to the ARG.B01 seismic power. The overlapping period of mid-June 2018 is used to adjust, over a 9 days time window, the ARG.B02 seismic power to the ARG.B01 seismic power.

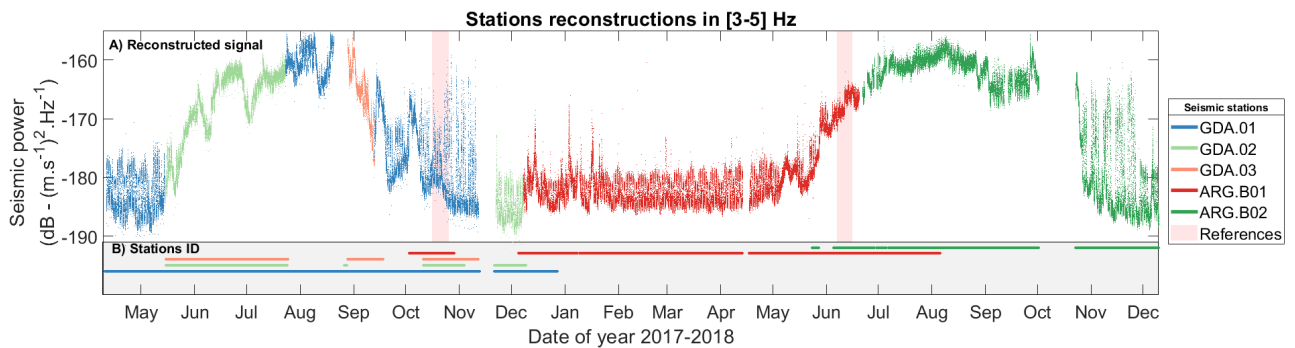


**Figure S1.** Time series of the corrected and assembled seismic power within the [3-5] Hz frequency range. We used this range to assemble the five stations seismic signals and apply the baseline shifts. Color coding refers to the corresponding stations and stations period of activity are shown in the light grey horizontal band. Light red vertical bands show the period used to constrain the baseline shift.

**S1.2 Evaluating instrumental bias in  $\delta t$  interpretation**

The subglacial channel-flow-induced seismic power  $P_w$  comparison between the different stations of our seismic network (Fig. 2) is shown in Fig. S2. We do not observe a significant time lag ( $< 5$  min) between  $P_w$  measured at 2 stations 200 m apart (GDA.02 and GDA.03). It is important to note that this lag time  $\delta t_{inst}$  does not directly correspond neither to the water transit time, nor to the water flow speed between our instruments. This effect is mainly related to the seismic waves properties when propagating within the glacier. Our analyses is important for the intra-diurnal time scale, because this means that if  $Q$  and  $P_w$  are out of phase by more than  $\delta t_{inst} = 15$  min (because  $Q$  measurement is done 600 m away from the seismic station) then this delay expresses subglacial hydraulic properties.

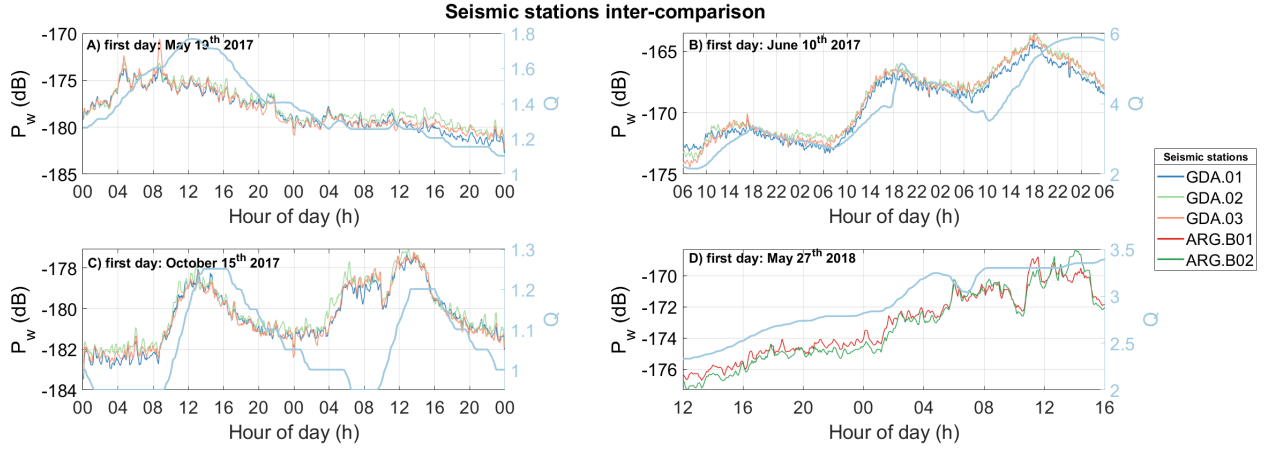


**Figure S2.** Time series of the measured seismic power within [3-7] hz at the different stations. (a) and (b) for the GDA network and (c) and (d) for the ARG network. Measurement is smoothed over 15 minutes, with one point every 15 minutes.

### S1.3 Evaluating the potential bias from impulsive events contribution to seismic power

Over alpine glacier, impulsive events can be of diverse origins from serac falls (Roux et al., 2008), crevasses opening (e.g. Neave and Savage, 1970; Lindner et al., 2019), hydraulic fracturation, microseismicity linked with water discharge (Iken and Bindschadler, 1986; Preiswerk and Walter, 2018) or even basal stick-slip events as recently shown on Glacier d'Argentière by (Helmstetter et al., 2015). It is crucial to limit the influence of such impulsive events when aiming to study the subglacial channel-flow-induced seismic power. With respect to water tremor, impulsive events are characterized by short time-scale amplitude burst above the noise level by up to several order of magnitude. An important parameter for the Welch method is the time period  $dt$  over which we compute the Fourier transform  $FT$ . The seismic power  $P$  is calculated as  $P = 10 \times \log_{10} \left[ \left( \frac{FT}{dt} \right)^2 \right]$ . The longer  $dt$ , the greater number of impulsive events have the chance to occur. And the more the impulsive events within  $dt$ , the more they influence  $P$  and hidden the turbulent water flow source. The size of this window is limited by the frequencies investigated. To limit the impulsive events influence and still be able to investigate a frequency range down to 1 Hz we have chosen for our study a  $dt = 2$  sec.

### S1.4 Evaluating the anthropogenic signature influence on sub-diurnal timescales

Because the anthropogenic noise power presents a well-marked diurnal variability that could bias the analyses of the  $P_w$  analyses, we determine, from visual inspection in Fig. S3, the period during which  $P_w$  dominates the seismic power as averaged within [3-7] Hz frequency range.

### S1.5 Evaluating the spatial sensitivity of the seismic record

During their journey from the source to the seismic station, seismic waves are attenuated. This behavior is related to energy dissipation within the propagation medium, here the ice, and because the higher the source to station distance, the larger the traveling distance and the thus lower the signal energy is. The attenuation of a signal with an amplitude of  $P_0$  is defined as:

$$P_d = P_0 \frac{1}{d^n} e^{-\frac{2\pi df}{v_c Q}}, \quad (S1)$$

with  $d$  the distance from the source,  $n$  the geometrical exponent with  $n=1$  for surface waves and  $n=2$  for body waves,  $f$  the considered frequency,  $v_c$  the waves propagation velocity and  $Q$  the quality factor. The higher  $Q$  the more dissipative the medium is. Numerous values of  $Q$  have been proposed for alpine glacier ice within our frequency range, from  $Q=6 \pm 1$  when considering only the uppermost glacier ice (first meters, Gusmeroli et al., 2010) up to  $Q=70$  for the 100 to 500 m layer (Kohnen, 1969). For our investigation we cover  $Q = [5, 20, 60, 100]$ . We seek here to quantify the area around our seismic stations that can contribute within a certain energy, here 10 dB, to the measured seismic power  $P_{mea}$ . We investigate two cases with a closest source  $S_1$  located at  $d_1 = 1$  and  $d_1' = 200$  m from the sensor. The former would represent a surface source, the latter a basal one at the glacier basis. We then searched for the distance  $d(S_1, S_2)$  between the closest source  $S_1$  and a second

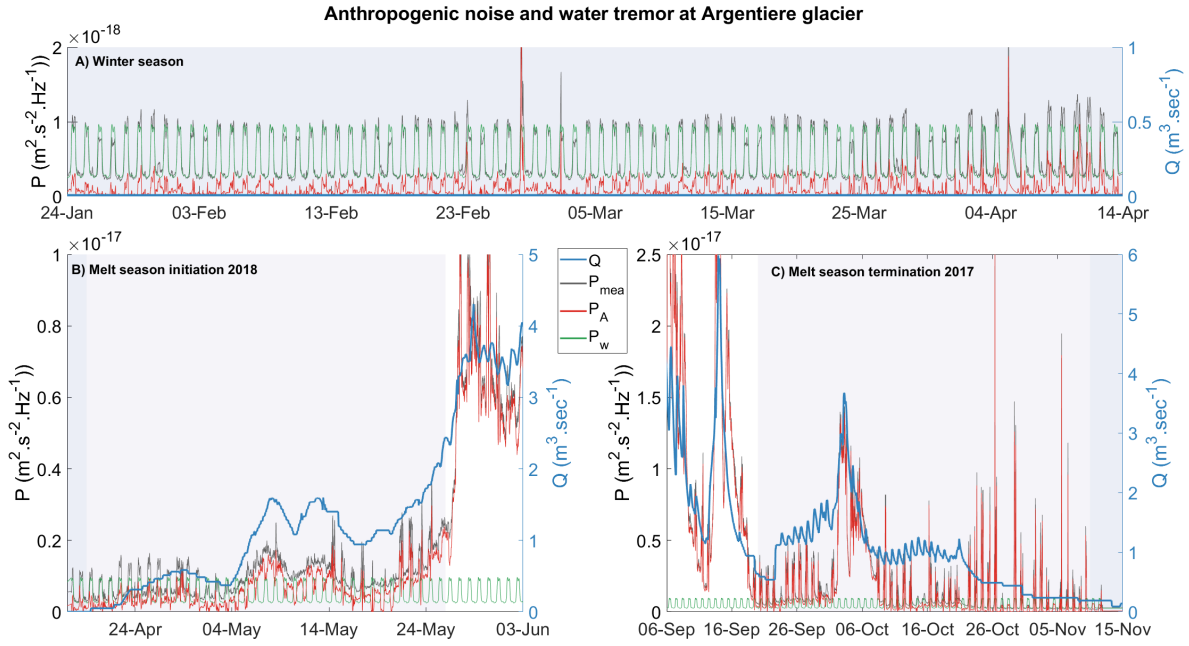


**Figure S3.** Time series of the measured seismic power ( $P_{mea}$ , grey line), the daily-fitted anthropogenic noise seismic power ( $P_A$ , green line), the computed water tremor ( $P_w = P_{mea} - P_A$ , red line) and the measured water discharge ( $Q$ , blue line). The three periods ( a) winter season, b) melt season initiation and c) melt season termination) presented are key to characterize the relative contributions of  $P_A$  and  $P_w$  to  $P_{mea}$ . Shaded blue area represents the hydrological winter period where  $Q < Q_{lim}$ , light shaded blue area represents the period where the diurnal anthropogenic spectral is too pronounced to study  $P_w$  on a daily basis. x and y axis scale are not correspondent between the panels.

one  $S_2$  where  $P_{S_1,mea} - P_{S_2,mea} = 10$  dB. This threshold value represent a relative value of 10% with respect to energy emitted from  $S_1$  with no consideration of the absolute energy.

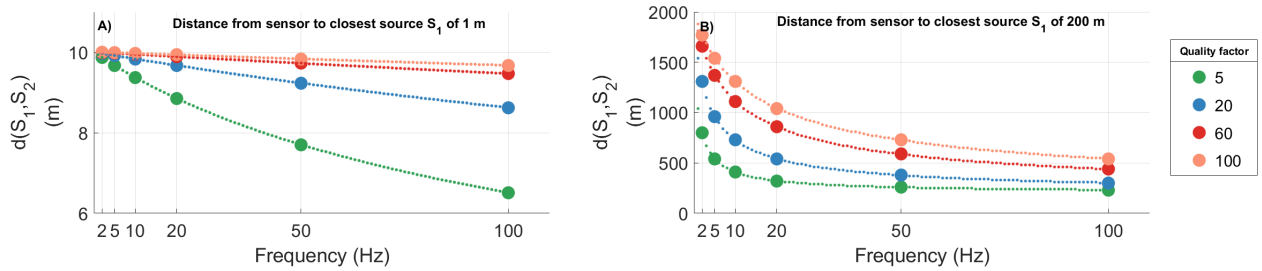


**Figure S4.** Synthetic effect of attenuation on seismic surface wave ( $n=1$ ). The two panels show the distance  $d(S_1, S_2)$  of a source  $S_2$  to the closest source  $S_1$  where the attenuation is such that  $P(S_1)_{sensor} = (S_2)_{sensor} + 10$  dB depending on the frequency and the quality factor. This distance represents the radius of source location within which any given source will contribute for at least 10% to the recorded seismic power with respect to a source located at distance of 1 m (left panel) and 200 m (right panel ) from the sensor.

Figure S4 (a) shows that with respect to a surface source  $S_1$  located at 1 m from the sensor, only the sources within a 10 m radius area will contribute to the [3-7] Hz signal energy by 10 dB, 10%, with respect to  $S_1$ . This area is reduced for increasing frequencies and quality factor. When we consider a source located at the glacier basis (Fig. S4 (b) ), we observe that all sources within 500 to 1500 m from the sensor would contribute to the [3-7] Hz signal energy by 10%. The frequency and the quality factor effect is now dominated by the exponential decrease from equation S4. These results shows that if we consider water tremor signal within [3-7] Hz, a quality factor of  $Q=20$ , and a closest source at the glacier base then the measured signal will be dominated by sources located within a radius of 800 m from our sensor.

5

10

## S2 Theoretical channel properties

### S2.1 Evaluating theoretical channels dynamics with Röthlisberger (1972)' equations

In his paper, Röthlisberger (1972) proposes the two following equations for steady-state channels at equilibrium:

$$4R^2 = \left( \frac{2^{4/3} \rho_w g}{\pi^2} \right)^{3/8} k^{-3/4} Q^{3/4} \left( \frac{dp}{dx} \right)^{-3/8} \quad (S2)$$

$$\frac{dp}{dx} = Bk^{-6/11} (nA^{-8n/11} Q^{-2/11} (P-p)^{8n/11}), \quad (S3)$$

with  $\frac{dp}{dx}$  the hydraulic pressure gradient  $S$ ,  $P$  the cryostatic pressure,  $k$  the channel roughness,  $B$  equals to constant,  $A$  and  $n$  ice flow parameters. Taking equation S3 and considering constant effective pressure ( $P-p$ ) and flow parameters leads to

$$S \propto Q^{-2/11}.$$

Now inserting equation S3 in S2 and considering constant channel roughness, leads to

$$\begin{aligned} R^2 &\propto Q^{3/4} \left( Q^{-2/11} \right)^{-3/8}, \\ R^2 &\propto Q^{66/88} Q^{6/88}, \\ R^2 &\propto Q^{9/11}, \\ R &\propto Q^{9/22}. \end{aligned}$$

For a steady-state channel not in equilibrium with  $Q$  that responds solely through changes in  $S$  this leads to

$$\begin{aligned} S^{3/8} &\propto Q^{3/4}, \\ S^{3/8} &\propto Q^{6/8}, \\ S &\propto Q^2. \end{aligned}$$

### S2.2 Evaluating theoretical melt and creep rates with Hooke (1984)' equations

We use here equations 6 and 8 of Hooke (1984) to evaluate the theoretical melt rate  $\dot{m}$  and creep rate  $\dot{r}$ , which are as follows

$$\dot{m} = C_2 Q^{3/5} \sin(\beta)^{6/5}, \quad (S4)$$

$$\dot{r} = C_3 \frac{Q^{2/5}}{\sin(\beta)^{1/5}} H^3, \quad (S5)$$

with  $H$  the ice thickness,  $\beta$  the surface slope,  $C_2$  and  $C_3$  constant. We use the values of Hooke (1984) for the two constants:  $C_2 = 3.731e^{-5} \text{ m}^{-4/5} \text{ s}^{-2/3}$  and  $C_3 = 5.71e^{-14} \text{ m}^{-16/5} \text{ s}^{-3/5}$ . We show in Fig. S5 the theoretical channel growth rate for a R-channel at steady state. Calculations are made following Eqs. (S5) and (S4). The equilibrium condition, melt rate equals creep rate, is verified when the channel growth rate equals zero. This shows that for a given glacier geometry (slope and thickness), the equilibrium condition depends only on the water discharge. The more the channel number, the less the discharge per channel for a given output discharge and therefore the longer the equilibrium condition can be satisfied.

We show in Fig. S6 the synthetic closure rate of an open channel and compared it to the observed channel radius changes, assuming that the hydraulic radius changes equals the channel radius changes. Our comparison show that for the observed range of channel radius changes (5 to 10 %) the channel response time is of about a couple of hours. Therefore channel could creep fast enough at sub-diurnal timescale to equilibrate channel growth by melt.

We estimate melt and creep rates using equations 6 and 8 of Hooke (1984) as here above. From mid-May to early July, hydraulic radius  $R$  increases by a factor of 3 to 4. For constant number of channels, this results in summer channels radius

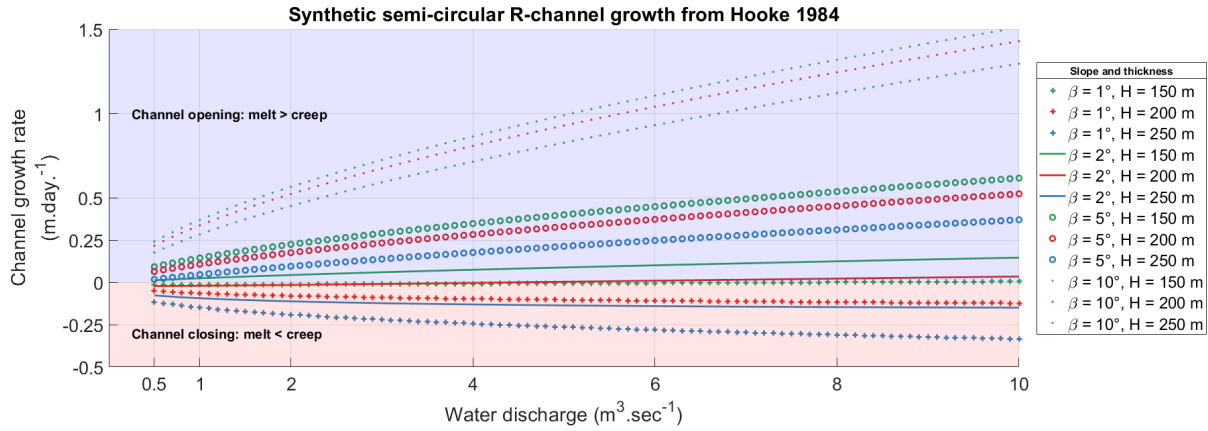


**Figure S5.** Synthetic evolution of a semi-circular shaped R-channel. Melt ( $\dot{m}$ ) and creep ( $\dot{r}$ ) rate are calculated from Eqs.( S5) and ( S4) of Hooke (1984) with the constants  $C_2$  and  $C_3$  as in Hooke (1984), the slope and the ice thickness are shown in the legend. The curves show  $\dot{m} - \dot{r}$ , with the shaded blue area  $\dot{m} > \dot{r}$  and the shaded red area  $\dot{m} < \dot{r}$ .

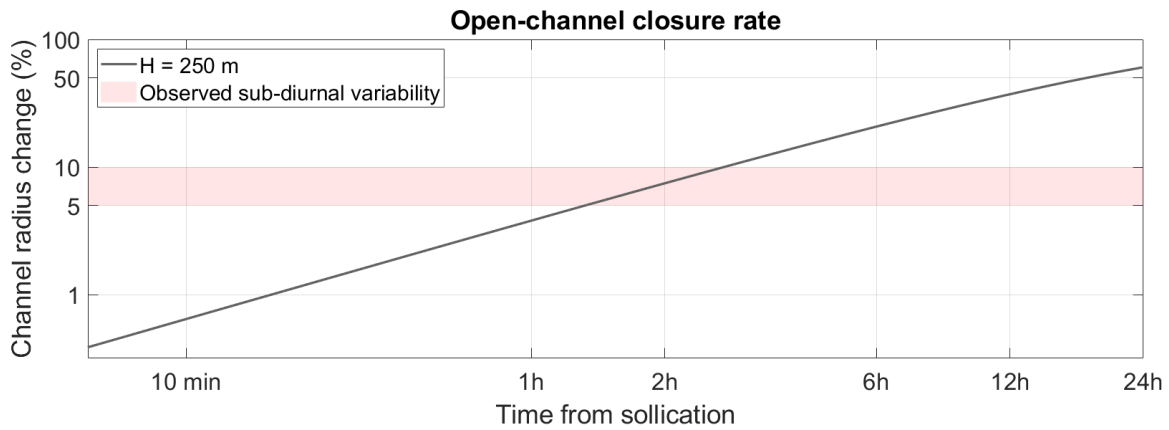


**Figure S6.** Synthetic closure rate of an open-channel computed for a channel size  $R(t) = R_0 e^{(-c\sigma_i^n t)}$ , with  $R(t)$  the channel radius through time,  $R_0$  the initial channel size,  $c = 1e^{-24} \text{ Pa}^{-3} \cdot \text{s}^{-1}$  the ice viscosity (Cuffey and Paterson, 2010),  $n = 3$  the Glen’s flow constant (Cuffey and Paterson, 2010) and  $\sigma = \rho_i g h_i$  with  $\rho_i = 900 \text{ kg} \cdot \text{m}^{-3}$  the ice density,  $g = 9.81 \text{ m} \cdot \text{s}^{-2}$  the acceleration due to gravity and  $h = 250 \text{ m}$  the glacier thickness. The time is defined with  $t = 0$  the moment when channel become open (free flow) and the change are expressed in % with respect to the initial size, 10% being  $R(t) = R_0 \times 0.9$ . Shaded red area shows the observed sub-diurnal variability in hydraulic radius at Glacier d’Argentière during summer of years 2017 and 2018.

of [1.00 - 1.25] m. Over the summer  $R$  varies by 4 to 8 % on a daily basis, which corresponds to diurnal changes of [4 - 10]  $\text{cm} \cdot \text{day}^{-1}$  in channel radius. Such changes are on the same order of magnitude as those calculated with Hooke (1984) equations which predict a melt rate of about [10-25]  $\text{cm} \cdot \text{day}^{-1}$  and creep rate of about [5-20]  $\text{cm} \cdot \text{day}^{-1}$  for these periods ( $Q \propto 5 \text{ m}^3 \cdot \text{sec}^{-1}$ ). This shows that subglacial channels have the capability to adjust their size on a daily basis in response to water input variability. Channels can thus rapidly close during the water discharge decrease and possibly keep a closed-flow behavior over summer. This supports the plausibility the channels’ diurnal dynamic proposed previously based on our observations.

### S3 Codes for seismic processing

We show here our two codes used to process the raw SAC seismic data.

#### Listings

1	Code to correct SAC files from instrumental response . . . . .	S6
5	2 Code to compute PSD from 1 day SAC files . . . . .	S6

#### S3.1 Remove instrumental response with SAC

```

1 #!/bin/bash
2 # =====
3 # -----
10 path2dat=/media/ugonanni/2E3D-8697/DATA/ARGENTIERE/ARG_Borehole_Ugo
5 path2sac=$path2dat/SACt
6 path2sacday=$path2sac/DAY
7 path2saccorr=$path2sac/Corr
8 # -----
15 cd $path2sacday
10 ls A*.SAC > sac_list # list of all data
11
12 for file in `cat sac_list`;do
13     new_file=`echo $file | sed -e 's#DAY.SAC#DAY_Corr.SAC#g' ` \
120     echo $new_file
15     echo $file
16
17 sac <<EOF
18 setbb pzfile "./PZ.ARG.B01.normgain3_A0625" # PZ files for corrections
125 r $file
20 rmean
21 rtr
22 taper w 0.00001
23 trans from polezero S %pzfile to vel freqlim 0.25 0.5 450 490
230 w $new_file
25 quit
26 EOF
27 mv $new_file $path2saccorr/.
28 done

```

**Listing 1.** Code to correct SAC files from instrumental response

#### 35 S3.2 Compute PSD with Python

```

1 #!/usr/bin/env python3
2 @author: ugonanni
3
4 # -----
40 # Import packages
6 # -----
7
8 import glob
9 import matplotlib.pyplot as plt
145 import numpy as np
11 import obspy
12 from os.path import join
13 from obspy.core import read
14 from obspy.core import UTCDateTime
150

```

```
16 from scipy.signal import welch, hanning
17 from scipy import signal
18
19 import os
20
21 import scipy
22 import scipy.fftpack
23
24 from scipy import pi
25 from scipy.fftpack import fft
26
27 import time
28
29 import astropy.time
30 import dateutil.parser
31
32 import datetime
33 import pandas as pd
34 # -----
35 # Define path
36 # -----
37
38 path2dat = '/media/ugonanni/Nanni/DATA_ARG_backup/GDA/SAC/RAW'
39 path2sav = '/home/ugonanni/Share/PhD/DATA/PWelch_output'
40
41
42 filename = ''
43
44 # -----
45 # Define parameters
46 # -----
47
48
49 # Pwelch parameters
50 l_win = 4 # secondes
51 # window
52 window = 'hanning'
53 # detrend
54 detrend = 'False'
55 # Number of segments
56 nb_seg = 2**19
57 lseg = l_win/2
58
59
60 # Initialize PSD vector
61 len_PSD = 1001
62
63
64 # min and max frequency to select frequency bands
65 fmin = [1,5,10,20]
66 fmax = [5,10,20,50]
67
68 # define time according to first day of 2017, i.e. DOY 2017
69 time17 = astropy.time.Time(datetime.datetime(2017, 1, 1, 0, 0))
70
71 t17 = time17.jd-1
72
73 # -----
74 # Compute PWelch
```

5

10

15

20

25

30

35

40

45

50

55

```

75 # -----
76
77 it_day = 0
78 # select file type
79
80 for ext in ['*03..1Z*']:
81
82     nbfiles = len(glob.glob(path2dat + '/' + ext))
83     for file in sorted(glob.glob(path2dat + '/' + ext)):
84
85         # read data and time
86         data = read(file)
87         Time_data = data[0]
88
89
90         # define names
91         t = Time_data.stats.starttime
92         name = '' + Time_data.stats.network + '.' + Time_data.stats.station + '.' +
Time_data.stats.channel + '.' + str(t.year) + '.' + str(t.month) + '.' + str(t.day)
93         print(name)
94
95
96         # File duration in secondes
97         duration = Time_data.stats.endtime - Time_data.stats.starttime
98
99         # Sampling frequency of the time series.
100         fs = int(np.round(Time_data.stats.sampling_rate))
101
102         # number of points of the data
103         nb_psd = duration/l_win
104
105         # define PSD matrix
106         PSD_matrix = np.empty([int(nb_psd), int(len_PSD)])
107         Time_vector = []
108         Hydro = np.empty([int(nb_psd), len(fmin)])
109         Hydro_std = np.empty([int(nb_psd), len(fmin)])
110
111         # compute PSD
112         for jj in range(0, int(nb_psd)):
113             # extract short time
114             tmp = Time_data[jj*l_win*fs:(jj+1)*l_win*fs]
115             nb_points = len(tmp)
116
117             # Length of each segment.
118             nperseg = fs*lseg # here 1 secondes
119
120             # Number of points to overlap between segments.
121             noverlap = nperseg / 2
122
123             # Time associated with Pwelch is centered on the window
124             a = int(((jj*l_win)+(l_win/2)))
125
126             Time_vector.append(Time_data.stats.starttime + a)
127
128
129             # Compute PSD with welch
130             if nb_points >= nperseg:
131                 f, Pxx = welch(tmp, fs, window=window, nperseg=nperseg, noverlap=noverlap,
detrend=False, return_onesided=True)

```



```

132         PSD_matrix[jj,:] = Pxx
133
134
135     Time_vector = np.asarray(Time_vector)
136
137     Tdoy = np.empty(len(Time_vector))
138     for jj in range(0,len(Time_vector)):
139         tim = astropy.time.Time(datetime.datetime(Time_vector[jj].year, Time_vector[jj].
140 month, Time_vector[jj].day, Time_vector[jj].hour, Time_vector[jj].minute, Time_vector[jj]
141 ].second))
142         Tdoy[jj] = tim.jd
143     Tdoy = Tdoy - t17
144     #plt.plot(Time_data)
145     #plt.show()
146
147     print(str(it_day+1) + ' over ' + str(nbfiles))
148     it_day = it_day + 1
149     # save data
150     try:
151         np.savetxt(path2sav + '/' + name + '_PSD_Tcorr_' + str(l_win) + 'sec', PSD_matrix)
152         np.savetxt(path2sav + '/' + name + '_Time_Tcorr_' + str(l_win) + 'sec', Tdoy)
153     except IOError:
154         print("Not enough space")
155         os.system('pause')
156         # We try again
157     try:
158         np.savetxt(path2sav + '/' + name + '_PSD_Tcorr_' + str(l_win) + 'sec',
159 PSD_matrix)
160         np.savetxt(path2sav + '/' + name + '_Time_Tcorr_' + str(l_win) + 'sec', Tdoy)
161     except IOError:
162         print("Still not enough space")
163
164
165
166     np.savetxt(path2sav + '/' + name + '_Frequency_Tcorr_' + str(l_win) + 'sec', f)
167
168     # loop on each days for concatenating

```

**Listing 2.** Code to compute PSD from 1 day SAC files

## References

- Cuffey, K. M. and Paterson, W. S. B.: The physics of glaciers, Academic Press, 2010.
- Gusmeroli, A., Clark, R. A., Murray, T., Booth, A. D., Kulessa, B., and Barrett, B. E.: Seismic wave attenuation in the uppermost glacier ice of Storglaciären, Sweden, *Journal of Glaciology*, 56, 249–256, 2010.
- Helmstetter, A., Nicolas, B., Comon, P., and Gay, M.: Basal icequakes recorded beneath an Alpine glacier (Glacier d’Argentière, Mont Blanc, France): Evidence for stick-slip motion?, *Journal of Geophysical Research: Earth Surface*, 120, 379–401, 2015.
- Hooke, R. L.: On the role of mechanical energy in maintaining subglacial water conduits at atmospheric pressure, *Journal of Glaciology*, 30, 180–187, 1984.
- Iken, A. and Bindshadler, R. A.: Combined measurements of subglacial water pressure and surface velocity of Findelengletscher, Switzerland: conclusions about drainage system and sliding mechanism, *Journal of Glaciology*, 32, 101–119, 1986.
- Kohnen, H.: Über die Absorption elastischer longitudinaler Wellen im Eis, *Polarforschung*, 39, 269–275, 1969.
- Lindner, F., Laske, G., Walter, F., and Doran, A. K.: Crevasse-induced Rayleigh-wave azimuthal anisotropy on Glacier de la Plaine Morte, Switzerland, *Annals of Glaciology*, 60, 96–111, 2019.
- Neave, K. and Savage, J.: Icequakes on the Athabasca glacier, *Journal of Geophysical Research*, 75, 1351–1362, 1970.
- Preiswerk, L. E. and Walter, F.: High-Frequency (> 2 Hz) Ambient Seismic Noise on High-Melt Glaciers: Green’s Function Estimation and Source Characterization, *Journal of Geophysical Research: Earth Surface*, 123, 1667–1681, 2018.
- Röthlisberger, H.: Water pressure in intra-and subglacial channels, *Journal of Glaciology*, 11, 177–203, 1972.

Roux, P.-F., Marsan, D., Métaixian, J.-P., O'Brien, G., and Moreau, L.: Microseismic activity within a serac zone in an alpine glacier (Glacier d'Argentiere, Mont Blanc, France), *Journal of Glaciology*, 54, 157–168, 2008.